



Double blue zones in inverse and normal laminar jet diffusion flames

Zhengyang Wang^a, Peter B. Sunderland^{a,*}, Richard L. Axelbaum^b

^a Department of Fire Protection Engineering, University of Maryland, 3104 J.M. Patterson Building, College Park, MD 20742, USA

^b Department of Energy, Environmental and Chemical Engineering, Washington University in St. Louis, St. Louis, MO 63130, USA

ARTICLE INFO

Article history:

Received 11 June 2019

Revised 18 July 2019

Accepted 16 September 2019

Keywords:

Chemiluminescence

Deconvolution

Spectroscopy

Triple flames

ABSTRACT

Past experimental and computational works indicate that double blue zones are possible in hydrocarbon diffusion flames. This study examines these zones in inverse (IDF) and normal (NDF) laminar gas jet diffusion flames. Over 100 diffusion flames were observed with various fuels, diluents, dilution levels, and flow rates. Upon close examination, the IDFs and NDFs are seen to have double blue zones, separated at the flame tip by up to 1.6 and 0.9 mm, respectively, with a relatively dark region in between. By partially premixing the fuel and oxidizer streams, it was observed that, for both IDFs and NDFs, the zone toward the fuel side is rich, while that toward the oxidizer side is stoichiometric. Chemiluminescence was investigated using cameras and bandpass filters emphasizing emissions from OH* (310 nm), CH* (430 nm), CO₂* (455 nm), and C₂* (515 nm). The images were deconvolved using onion peeling. Broadband CO₂* emissions were subtracted from the images of OH*, CH*, and C₂* emissions to find profiles of spectral emissive power for these species. The thin, blue-green zone on the fuel side coincides with the peaks in CH* and C₂* emissions in the fuel-consumption zone, while the broader, blue stoichiometric zone coincides with the peaks in OH* and CO₂* emissions in the oxygen-consumption zone. The spectral emissive power peaks for C₂*, CO₂*, CH*, and OH* are typically 3 times as high in the IDF as in the NDF, which is attributed to the higher scalar dissipation rates.

© 2019 The Combustion Institute. Published by Elsevier Inc. All rights reserved.

1. Introduction

The simplest perspective of visual observation of hydrocarbon diffusion flames includes a thin blue reaction zone, often overshadowed by yellow emission from soot. However, previous research (experimental, analytical and computational) indicates that two blue zones (i.e., double blue zones) are possible.

Many published color images of inverse laminar jet diffusion flames (IDFs) reveal two blue zones separated by a thin dark region. These zones have been observed under a wide range of conditions, including various fuels, e.g., CH₄, C₂H₄, C₂H₆, and C₃H₈; normal gravity flames [1–8]; microgravity flames [9–13]; coflow flames [1,2,6–9]; jet flames in quiescent ambients [11–13]; attached flames [1,3–13]; and lifted flames [2]. Only one past study mentioned these zones [5].

Double blue zones are also observable in normal laminar jet diffusion flames (NDFs). Gülder and co-workers [14,15] reported a two-zone structure in methane-oxygen flames. An inner blue region was surrounded by widely distributed blue haze. Saito and co-workers [16,17] reported similar behavior in methane-air

flames. Weinberg and co-workers [18,19] observed distinct double blue zones in methane and natural gas NDFs. All these studies [14–19] attributed the zone towards the fuel to hydrocarbon oxidation and the zone towards the oxidizer to CO and/or H₂ oxidation.

Sung et al. [10] observed double luminous zones in CH₄-doped H₂ spherical inverse diffusion flames. The zones were separated by up to 8 mm. The zone toward the fuel was blue-green and was attributed to C₂* emission from CH₄ consumption. The zone toward the oxidizer was blue and was attributed to CO₂* emission from H₂ consumption. The double zones only occurred for CH₄ fuel mole fractions of 1.5–9.5%.

Double blue zones in diffusion flames may arise because the product and intermediate concentrations do not have coincident peaks. For example, in methane-air IDFs and NDFs, the concentrations of H₂, C₂, CH, and CO peak on the rich side of stoichiometric [20–23], whereas in the NDFs, CO₂, OH, and temperature peak at stoichiometry or on the lean side [20–22].

The above observations are consistent with the predictions of rate-ratio asymptotics [24–26] for methane diffusion flames. In particular, a fuel-consumption zone (toward the fuel side) produces CO and H₂ and an oxygen-consumption zone (toward the oxidizer side), somewhat thicker [25], produces CO₂ and H₂O. This behavior constitutes a “diffusion flame within a diffusion flame” [26].

* Corresponding author.

E-mail address: pbs@umd.edu (P.B. Sunderland).

Table 1
The bandpass filter wavelengths and transmittances, the associated species, the cameras used, and parameters α , β and γ of Eq. (6). The filters are bandpass filters from Andover Corp. and have FWHMs of 10 nm.

Filter central λ (nm)	Filter peak τ	Species	Camera(s) used	α	β	γ
310	0.15	OH*	ICCD	0.33	0.67	0.24
430	0.46	CH*	CCD	1	0.89	0.73
455	0.63	CO ₂ *	ICCD & CCD	1	1	1
515	0.65	C ₂ *	CCD	0.67	0.75	1.03

Double blue zones were observed near the anchoring points of hydrocarbon diffusion flames [27], but soot luminosity prevented determining whether this was a localized phenomenon associated with reactant leakage at the quenched flame base.

Most of the visible emissions in soot-free hydrocarbon flames come not from stable species but from excited-state C₂*, CO₂* CH*, and OH* [28]. Most past measurements of flame chemiluminescence were in premixed flames, for which chemiluminescence from these species peaks near the flame front [29–32]. Diao et al. [17] found the emissions of CH* and C₂* to be coincident and to arise from nearly stoichiometric regions of methane-air diffusion flames. Other studies of flame chemiluminescence in diffusion flames away from anchoring points had either too much soot interference [27,33] or too low spatial resolution [30,34,35] to resolve possible double blue zones.

Much remains unknown about double blue zones in diffusion flames. For single-component fuels, it is not known where these zones reside relative to the stoichiometric region. It is unknown which species are responsible for the double zones, and whether they appear in all laminar hydrocarbon diffusion flames. To address this, the double blue zones in IDFs and NDFs are examined. Flame chemiluminescence from C₂*, CO₂* CH*, and OH* is investigated using filtered images and image deconvolution. The results contribute to an improved fundamental understanding of diffusion flame structure and insight into the visual identification of the stoichiometric zone and various species peaks in IDFs and NDFs.

2. Experimental

Diffusion flames were observed using a co-flow burner. The outer port had an inside diameter of 102 mm and contained ceramic honeycomb for uniform flow. It was sealed to a 155 mm long glass chimney whose outlet was covered with aluminum foil with a 15 mm round hole on axis for exhaust. Two different size inner ports were used, with inside diameters of 2.7 and 15 mm. Both were stainless steel and had a wall thickness of 0.68 mm and a discharge height of 5 mm above the honeycomb. For the IDFs, fuel flowed through the outer port and oxidizer flowed through the inner port, and for the NDFs these were reversed. For IDFs a secondary flame was ignited at the top of the chimney to consume the unburned fuel, but this had no effect on the IDFs. For diffusion flames, the outer gas flow rate was maintained at ten times the stoichiometric requirement. For some tests, partially premixed fuel and oxidizer was supplied to the inner and/or outer ports. All flames were laminar and steady.

The reactants were CH₄ (99.99%), C₃H₈ (99.5%) and O₂ (99.994%) and the diluents were Ar (99.999%), CO₂ (99.999%), He (99.999%), and N₂ (99.998%). Ambient conditions were 1.01 bar and 25 °C. Flow rates were controlled with metering valves and measured with calibrated rotameters. The flow rates had estimated uncertainties of $\pm 5\%$, but they were reproducible to within 1%.

The camera used for color imaging and imaging C₂*, CO₂* and CH* was a Nikon D100 charged-couple device (CCD) digital camera with 6 megapixels and a 60 mm AF Micro-Nikkor lens. The ISO (International Organization for Standardization) setting was 200 and the f-number (f) was 2.8. The exposure time, t , was varied between

0.003 and 30 s such that images were bright but without saturation at any pixel in any color plane. The white balance was direct sunlight, but this had no effect because the images were recorded in raw format. The front of the lens was 15 cm from the flame axis and its optical axis was 50 mm above the inner port. The pixel spacing in the object plane was 10 μ m.

The CCD images were recorded in raw format and converted to 3 \times 16 bit tif format using Ddraw (with default settings except -4 and $-T$) to avoid gamma corrections [36]. For each pixel the red (R), green (G), and blue (B) pixel values (I_R , I_G , and I_B) were extracted with MATLAB's `imread` and `im2double` functions. The dark-current pixel values, I_{DC} , were small (below 0.004 in each color plane) and had negligible variation with shutter time.

An ultra-violet (UV) camera was used to image OH* emissions. This was an intensified charge-coupled device (ICCD) camera (XY-BION Electronic System, ISG-250-GQU3) with 0.4 megapixels and a 105 mm Nikkor UV lens. This camera is sensitive to 180–900 nm. The intensifier gain was 2.5 V, f was 4.5, and t was 33 ms such that images were bright but without saturation at any pixel. The front of the lens was 40 cm from the flame axis and its optical axis was 50 mm above the inner port. The pixel spacing in the object plane was 17 μ m.

The UV video output was recorded at 30 frames/s to mp4 video using Elgato video capture. Still grayscale images, in 8 bit tif format, were obtained using VLC media player. For each pixel the grayscale pixel values (I_{ICCD}) were extracted as real values between 0 and 1 with MATLAB's `imread` and `im2double` functions. The dark-current pixel values were negligible.

A 50 mm round bandpass filter was placed in front of the CCD or ICCD camera lens for most images. Four such filters were paired with the cameras as shown in Table 1. The filters for OH*, CH*, and C₂* match chemiluminescence peaks for these species, while the filter for CO₂* is in a region of broadband CO₂* emissions [17,28–33].

Grayscale (GS) pixel values for the CCD camera were defined as

$$I_{GS} = (I_R + I_G + I_B)/3, \quad (1)$$

where I is pixel value. For both cameras normalized pixel values were defined as

$$NI_i = (I_i - I_{i,DC})f^2/t, \quad (2)$$

where DC is dark current and i denotes the camera and the color plane.

A blackbody furnace (Oriol 67032) was used to calibrate both cameras when paired with various bandpass filters. The blackbody had a 25 mm aperture diameter, a temperature of 1000 °C, a temperature accuracy of ± 0.2 °C, and an emissivity of $\varepsilon = 0.99 \pm 0.01$. This emissivity in the visible was confirmed for a similar blackbody [37]. For the CCD and ICCD cameras, the lenses were 15 and 40 cm away, respectively, and were focused on the blackbody aperture. For each CCD (and ICCD) image, a 200 \times 200 (and 100 \times 100) pixel region centered on the aperture was considered, which corresponded to 1% (and 8%) of the aperture area.

The pixel sensitivity associated with each camera, lens, and bandpass filter is defined here as

$$S_i(\lambda) = NI_i/[\varepsilon E_b(\lambda, T)\tau(\lambda)FWHM], \quad (3)$$

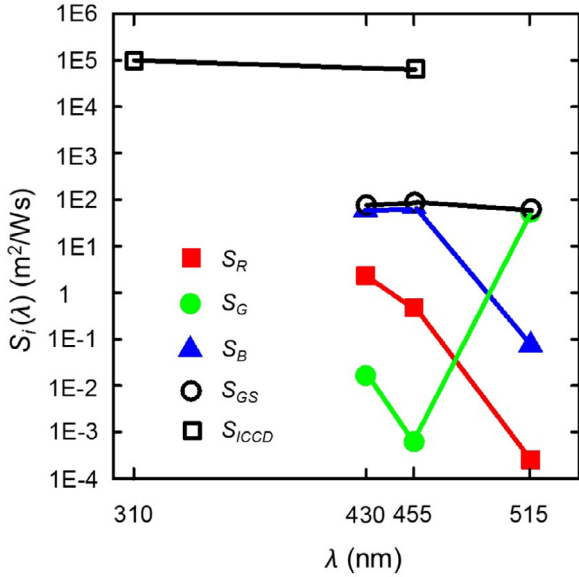


Fig. 1. Sensitivities of the CCD and ICCD cameras paired with filters.

where ε and T are the blackbody emissivity and temperature, λ , τ and $FWHM$ are the bandpass filter's central wavelength, peak transmittance, and full-width at half maximum (see Table 1), and E_b is the spectral emissive power of an ideal blackbody,

$$E_b(\lambda, T) = C_1 / \{ \lambda^5 [\exp(C_2 / \lambda T) - 1] \}, \quad (4)$$

where C_1 , and C_2 are the first and second radiation constants ($3.742 \times 10^{-4} \text{ W m}^2$ and $1.439 \times 10^4 \text{ } \mu\text{m/K}$).

Figure 1 summarizes the pixel sensitivities for each pairing of camera and filter. For the CCD camera this is consistent with past calibrations of similar CCD and complementary metal-oxide-semiconductor (CMOS) cameras [38,39]. Although the R, G, and B sensitivities vary with wavelength, the GS sensitivity is relatively constant.

For the ICCD camera paired with filters, the sensitivity was measured at 455 nm and estimated at 310 nm using this measurement and the camera and filter specifications. This was necessary because the blackbody emissions at 310 nm were too dim to be measured. This UV lens has relatively flat transmittance between 310 and 455 nm.

The ICCD has a higher sensitivity than the CCD owing to its intensifier array. The intensifier and bit depth of 8 add noise; at 455 nm the ICCD GS signal-to-noise ratio (the pixel value mean divided by its standard deviation) is 25, compared to 64 for the CCD.

Image deconvolution was performed because line-of-sight images of axisymmetric flames can complicate image interpretation. Deconvolution has been used widely to obtain properties such as soot temperature and soot volume fraction in axisymmetric flames [36,40] and more recently has yielded deconvolved flame images [29,33].

Onion peeling and Abel transforms are widely used deconvolution methods for combustion, e.g., [40–43]. The results generally agree, but for discrete signals Abel transforms yield singularities at the boundaries [41,42], e.g., on the centerline of axisymmetric flames. Onion peeling deconvolution was used here, for which the local property per unit length is the product of the projected property and the reconstruction matrix [40–43].

The deconvolution was performed separately for NI_R , NI_G , and NI_B from the unfiltered images, and for NI_{GS} from the filtered images. For both the filtered and unfiltered images, NI_i was smoothed in the horizontal direction using the Savitski–Golay filter function in MATLAB [41]. Parameters $\text{framelen}=51$ and $\text{order}=1$ were

specified, as they were found to suppress noise with minimal distortion of the intensity peaks. The flame images were split on the flame axis, deconvolved separately, and recombined.

After the filtered images from the CCD camera were converted to grayscale and deconvolved, the initial colors were approximately reproduced using

$$D(NI_i) = D(NI_{GS})S_i/S_{GS}, \quad (5)$$

where D is the deconvolution operator and i denotes R, G, or B.

The deconvolved results were converted to image files by scaling the values linearly to a range of 0–1 and then applying the MATLAB `imshow` function.

Extensive soot formation was avoided with diluents. However CO_2^* , like soot, has broad luminous emissions in the visible and UV [28–32]. To correct for this, images of CO_2^* emissions at 455 nm were used to estimate and subtract the contribution of CO_2^* emissions at 310, 430, and 515 nm. For both cameras, following deconvolution the correction applied at each pixel was

$$D(NI_{GS,\lambda,\text{corr}}) = D(NI_{GS,\lambda}) - \alpha_\lambda \beta_\lambda \gamma_\lambda D(NI_{GS,455\text{nm}}), \quad (6)$$

where corr denotes the correction for CO_2^* emissions. Parameters α , β , and γ are shown in Table 1. They are, respectively, the ratios of CO_2^* intensity, pixel sensitivity, and τ at wavelength λ divided by that at 455 nm. Parameter α comes from the measurements of Refs. [29,31,32] for methane–air diffusion flames, β comes from Fig. 1, and γ comes from the filter transmissivities.

At each pixel, the deconvolved spectral emissive power (E) for the species OH^* , CH^* , and C_2^* was found from

$$D[E(\lambda)] = D(NI_{GS,\text{corr},\lambda}) / [S_{GS}(\lambda)\tau(\lambda)FWHM], \quad (7)$$

while for CO_2^* quantity $NI_{GS,\lambda}$ replaced $NI_{GS,\text{corr},\lambda}$.

3. Results

The double blue zones were more prominent for IDFs than for NDFs, which perhaps explains why they have gone unnoticed for so long. They are also more prominent when Ar is used as the diluent. Figure 2(a) shows an image of a representative Ar-diluted methane IDF recorded by the CCD camera without a bandpass filter. Three main features are visible in this flame: (1) a broad (thick) blue inner zone that is closed at its tip; (2) outside of this a thinner, blue-green zone that appears open at the tip; and (3) outside of this a region of orange emissions from soot. The inner and outer zones are referred to here as the double blue zones and are identified with arrows in Fig. 2. The zones are closest low in the flame and diverge with increasing height. At the height where the inner zone closes on the axis, the outer zone is at a radius of 1.6 mm.

Quantity NI_{GS} was found for each pixel in the region shown by a white rectangle in Fig. 2(a). The values were averaged in the vertical direction within this region. The results are plotted in Fig. 2(a) and reveal that the inner blue zone is broad, the outer blue zone is narrow and brighter, and the soot region is outside the outer blue zone.

Figure 2(b) shows an image of a representative NDF. This flame also has double blue zones. Its inner zone is thin and blue-green and its outer zone is thicker and blue. Here again the zones diverge with increasing height. Both zones are closed on the flame axis (at the tip), where they are separated by 0.9 mm. Quantity NI_{GS} is also plotted for a similar region in this flame, indicating that the NDF's inner zone is narrower and brighter than its outer zone.

The blue zones in the IDF and NDF of Fig. 2 have several common features. The blue zone toward the fuel side is narrower, brighter, and blue-green, while that toward the oxidizer side is broader and dimmer. They also have some differences: in the IDF the double zones are brighter and more prominent and the outer zone is open on the flame axis.

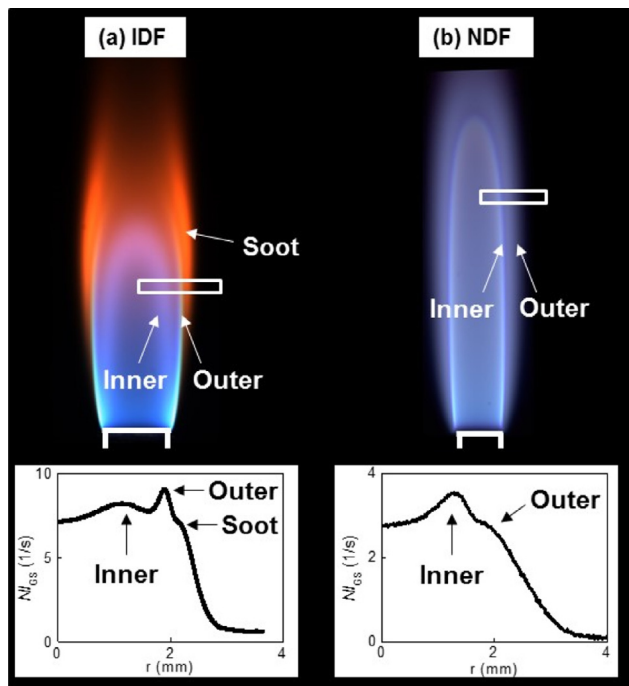


Fig. 2. Unfiltered CCD images of a representative Ar-diluted methane (a) IDF and (b) NDF. The IDF and NDF have flow rates of $\dot{m}_{O_2} = 5.2$ mg/s and $\dot{m}_{CH_4} = 1.63$ mg/s, methane mole fractions of $X_{CH_4} = 0.41$ and 0.19, and oxygen mole fractions of $X_{O_2} = 0.34$ and 0.32, respectively. The burner diameter is 2.7 mm.

Table 2
Conditions for the flames of Fig. 3.

Flame	Inner gas			Outer gas		
	\dot{m} mg/s	X_{CH_4}	X_{O_2}	\dot{m} mg/s	X_{CH_4}	X_{O_2}
a	6.06 ^a	0.07	0.30	52 ^b	0.60	0.11
b	6.06 ^a	–	0.32	52 ^b	0.60	0.11
c	6.06 ^a	–	0.32	52 ^b	0.67	–
d	0.41 ^b	0.26	0.21	35.2 ^a	0.04	0.23
e	1.26 ^b	0.19	0.22	35.2 ^a	–	0.45
f	1.26 ^b	0.28	–	35.2 ^a	–	0.45

^a Oxygen mass flow rate.

^b Methane mass flow rate.

Over 100 IDFs and NDFs, with little or no soot, were observed with various fuels (CH_4 , C_3H_8), diluents (Ar, N_2 , He, CO_2), stoichiometric mixture fractions (0.14–0.8), adiabatic flame temperatures (2052–2922 K), stoichiometric flame lengths (6–61 mm), and burner diameters (3 and 15 mm). All the flames exhibited double blue zones.

Partially premixing (i.e., adding oxidizer to the fuel and/or fuel to the oxidizer) can help identify whether the blue zones are lean, stoichiometric, or rich. Figure 3(a) shows a triple flame of $CH_4/O_2/N_2$ with conditions shown in Table 2. The outer gas is rich premixed and the inner gas is lean premixed. These flows support two premixed flames and a stoichiometric diffusion flame, as labeled in Fig. 3(a). As the flow rate of methane in the inner gas decreases, the rich premixed flame shortens until the double flame of Fig. 3(b) results. Here the two blue zones are identified as stoichiometric and rich. Next, as the flow rate of oxygen in the outer gas decreases there is little change in the appearance of the blue zones until the IDF of Fig. 3(c) results. This flame also has two blue zones, identified here as stoichiometric and rich.

Figure 3(a)–(c) indicate that the double blue zones of IDFs involve an inner stoichiometric zone and an outer rich zone. Additional support for this comes from OH planar laser-induced fluorescence measurements of methane and ethylene IDFs [44,45],

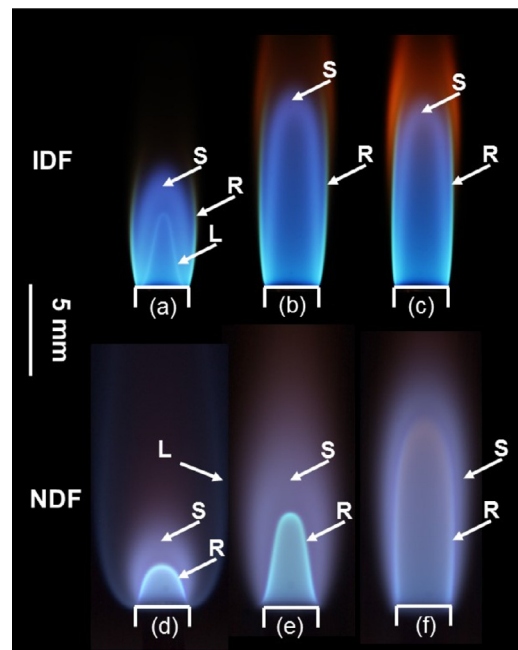


Fig. 3. Unfiltered CCD images of triple flames, double flames, and diffusion flames. (a) A triple flame with rich outer gas. (b) The double flame that results when methane is removed from the inner gas. (c) The IDF that results when, additionally, oxygen is removed from the outer gas. (d) A triple flame with lean outer gas. (e) The double flame that results when methane is removed from the outer gas. (f) The NDF that results when, additionally, oxygen is removed from the inner gas. The abbreviations are L (lean), R (rich), and S (stoichiometric).

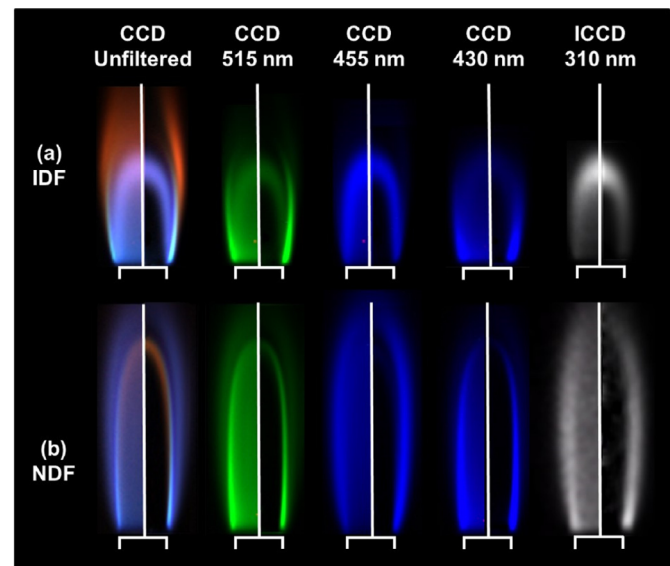


Fig. 4. Representative methane (a) IDF and (b) NDF images. The IDF and NDF have $\dot{m}_{O_2} = 4.02$ mg/s and $\dot{m}_{CH_4} = 1.26$ mg/s, $X_{CH_4} = 0.45$ and 0.28, and $X_{O_2} = 0.48$ and 0.38, respectively. Images to the right of each centerline are deconvolved. The burner diameter is 2.7 mm.

which found the stoichiometric regions to correspond with what we identify in their flame images to be the inner zones of IDFs.

Figure 3(d) shows another triple flame, but here the outer gas is lean premixed and the inner gas is rich premixed. These flows support two premixed flames and a stoichiometric diffusion flame, as labeled in Fig. 3(d). As the flow rate of methane in the outer gas decreases, the lean premixed flame widens until the double flame of Fig. 3(e) results. Here the two blue zones are identified as stoichiometric and rich, which is supported by similar tests [46,47].

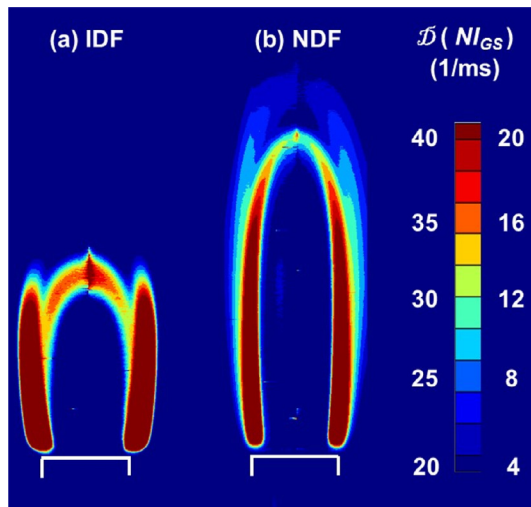


Fig. 5. Contour plot of deconvolved normalized intensities for the 515 nm filtered CCD images of Fig. 4. The values to the left and right of the color bar are for the IDF and NDF, respectively.

Next, as the flow rate of oxygen in the inner gas decreases the blue zones transition to those of Fig. 3(f), which is an NDF. This flame also has two blue zones, identified here as stoichiometric and rich.

Figure 3(d)–(f) indicate that the double blue zones of NDFs involve an outer stoichiometric zone and an inner rich zone. This finding is supported by similar tests performed in [48–50]. Note that most past flame shapes studies assumed the NDF inner zone to be stoichiometric, e.g., Ref. [9].

Figure 4(a) and (b) shows several views of an IDF and an NDF. The burner tip and centerline are shown in white. To the left and right of each centerline are the initial and deconvolved images.

Similar to the flames of Fig. 2, the unfiltered CCD images exhibit double blue zones for both the IDF and the NDF. When deconvolved, the flame features widen and their edges become sharper. Filtered images at all four wavelengths are also shown. The 515 nm images have the clearest double blue zones (which are green in Fig. 4 because the filter is green). The 430 nm images also have double blue zones, but only the rich zone is readily visible. The 455 and 310 nm images have only a single blue zone, corresponding to the stoichiometric zones in the unfiltered images.

Because the 515 nm images in Fig. 4 have the clearest double blue zones, these are examined further in Fig. 5 by presenting their

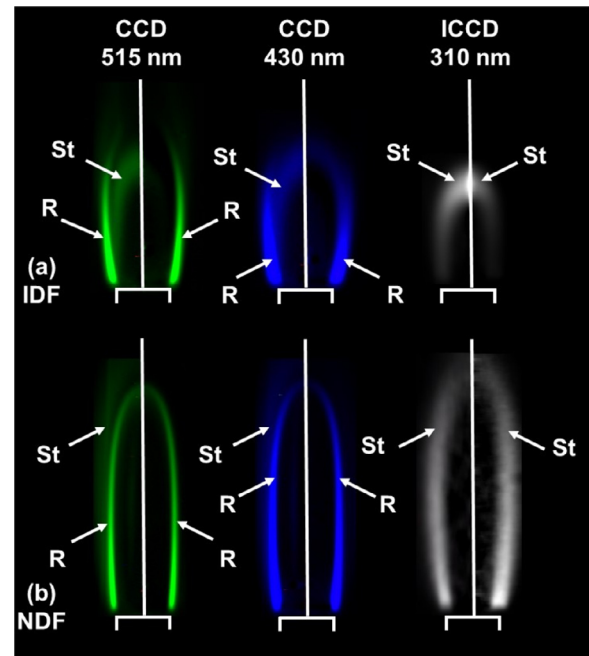


Fig. 6. Deconvolved images of filtered images before (left of axis) and after (right of axis) CO_2^* subtraction for the flames of Figs. 4 and 5.

$D(Nl_{GS})$ intensities as color contour plots. Both sides of the centerline are now shown. The double blue zones are more evident in the IDF. The peak intensities are much higher in the IDF. This is attributed to the increased scalar dissipation rates, as defined in [24–26], and temperatures.

Further interpretation of Figs. 4 and 5 is complicated by broadband CO_2^* emissions. Therefore subtraction of these emissions from the 515, 430, and 310 nm images was performed, with results shown in Fig. 6. To the left of each centerline is the deconvolved image of Fig. 4, and to right is the image following the subtraction of CO_2^* emissions. For the image at 310 nm the stoichiometric zone remains following subtraction. This is reasonable because both CO_2^* and OH^* (with emissions at 455 and 310 nm) are formed at or near the stoichiometric zone. For the images at 515 and 430 nm, the stoichiometric zones are now absent. This is reasonable because C_2^* and CH^* (with emissions at 515 and 430 nm) are formed on the rich side of stoichiometric. The appearance of a stoichiometric blue zone in the filtered images at 515 and 430 nm

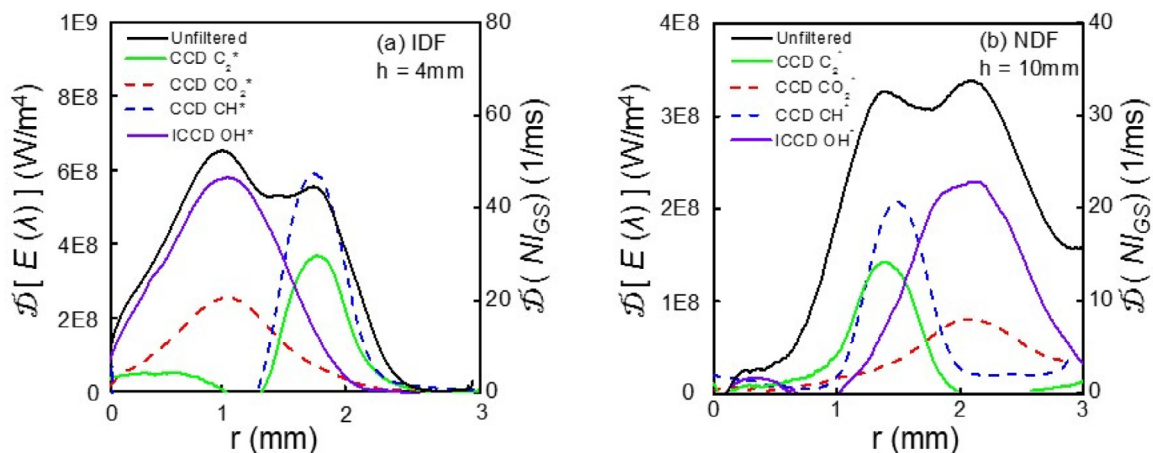


Fig. 7. Deconvolved spectral emissive power profiles of C_2^* , CO_2^* , CH^* and OH^* for (a) the IDF in Figs. 4–6 at a height of 4 mm and (b) the NDF in Figs. 4–6 at a height of 10 mm. The results for C_2^* , CH^* , and OH^* are after CO_2^* subtraction. The $D(Nl_{GS})$ profile for unfiltered CCD images at same flame height are also plotted.

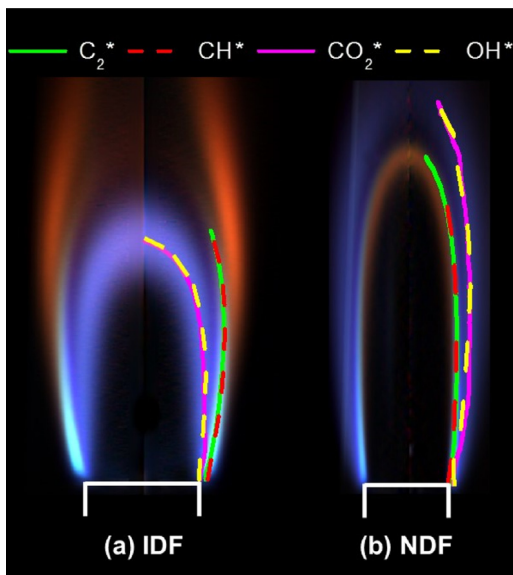


Fig. 8. The unfiltered images of Fig. 4 after deconvolution, and contours of peak $D [E_s (\lambda)]$ for four species. The results for C_2^* , CH^* , and OH^* are after CO_2^* subtraction.

resulted from CO_2^* interference. Thus, for both IDFs and NDFs, the peak emissions from C_2^* and CH^* are in the rich zone, whereas the peak emissions from CO_2^* and OH^* are in the stoichiometric zone.

Figure 7 shows the deconvolved spectral emissive power profiles for C_2^* , CO_2^* , CH^* and OH^* for representative heights in the two flames of Figs. 4–6. For both flames, the OH^* and CO_2^* emissions have coincident peaks near the stoichiometric zone, and C_2^* and CH^* emissions have nearly coincident peaks on the rich side. (The C_2^* peak is about 0.1 mm toward the fuel side as compared to the CH^* peak.) For both flames the highest $D [E (\lambda)]$ are for OH^* and CH^* and the lowest is for CO_2^* . All the peaks are about 3 times as high in the IDF as in the NDF, which is attributed to the higher scalar dissipation rates.

The $D (Nl_{GS})$ for unfiltered CCD images are also shown. These each have two peaks, of similar height, coincident with the other peaks in Fig. 7. Because OH^* has weak emissions in the visible, the unfiltered peak in the stoichiometric region results primarily from broadband CO_2^* emissions.

Figure 8 shows the unfiltered images of Fig. 4 after deconvolution, onto which are superimposed the contours of the peak deconvolved spectral emissive power of C_2^* , CO_2^* , CH^* and OH^* at each height. For both flames, the CH^* and C_2^* emissions are aligned with the rich zone, which makes it appear blue-green. For both flames the CO_2^* and OH^* emissions are aligned with the stoichiometric zone. Because OH^* emissions from flames are weak in the visible, the thick stoichiometric blue zone is primarily the result of CO_2^* emissions. These observations are consistent with the predicted existence from rate-ratio asymptotic of a fuel-consumption zone and an oxygen-consumption zone [24–26].

4. Conclusions

Double blue zones in both IDFs and NDFs were observed in over 100 hydrocarbon diffusion flames. Chemiluminescence associated with OH^* , CH^* , CO_2^* , and C_2^* was measured with 10 nm band-pass filters at 310, 430, 455, and 515 nm, respectively. The cameras with filters were calibrated with a blackbody furnace. Images were deconvolved by onion peeling and broadband CO_2^* emission was subtracted. The major conclusions are as follows.

1. Double blue zones are visible in all IDFs and NDFs without soot for various fuel reactants, diluents and burner diameters. These are more distinct in IDFs than in NDFs. The zones are separated by up to 1.6 mm (and 0.9 mm) at the flame tip for IDFs (and NDFs).
2. For both flame types, the blue zone toward the fuel side is rich and blue-green, while that toward the oxidizer side is stoichiometric, blue, and thicker. The rich blue zone results from emissions from CH^* and C_2^* in the fuel-consumption zone. The stoichiometric blue zone results from CO_2^* emissions in the oxygen-consumption zone and is coincident with the peak in OH^* .
3. For both flame types, the 430 and 515 nm images exhibit double blue zones, but emissions at these wavelengths in the stoichiometric region arise from CO_2^* interference. The 310 and 455 nm images exhibit only a single blue zone, this being in the stoichiometric region.
4. The deconvolved spectral emissive power peaks for C_2^* , CO_2^* , CH^* , and OH^* are about 3 times as high in the IDF as in the NDF, which is attributed to the higher scalar dissipation rates.

Declaration of Competing Interest

The authors declare that they have no known competing financial interests or personal relationships that could have appeared to influence the work reported in this paper.

Acknowledgments

This work was supported by NASA grants NNX15AC75A and NNX15AB60A, with Dennis Stocker as technical officer.

References

- [1] J. Walker, Flames in which air is introduced into a flammable gas rather than vice versa, *Sci. Am.* 241 (1979) 192–200.
- [2] J.H. Kent, H.G. Wagner, A reversed coflowing laminar diffusion flame, *Z. Phys. Chem.* 139 (1984) 59–68.
- [3] G.W. Sidebotham, I. Glassman, Flame temperature, fuel structure, and fuel concentration effects on soot formation in inverse diffusion flames, *Combust. Flame* 90 (1992) 269–272.
- [4] P.B. Sunderland, B.J. Mendelson, Z.G. Yuan, D.L. Urban, Shapes of buoyant and nonbuoyant laminar jet diffusion flames, *Combust. Flame* 116 (1999) 376–386.
- [5] P.B. Sunderland, S.S. Krishnan, J.P. Gore, Effects of oxygen enhancement and gravity on normal and inverse laminar jet diffusion flames, *Combust. Flame* 136 (2004) 254–256.
- [6] C.J. Unrau, R.L. Axelbaum, P. Biswas, P. Fraundorf, Synthesis of single-walled carbon nanotubes in oxy-fuel inverse diffusion flames with online diagnostics, *Proc. Combust. Inst.* 31 (2007) 1865–1872.
- [7] B.M. Kumfer, S.A. Skeen, R.L. Axelbaum, Soot inception limits in laminar diffusion flames with application to oxy-fuel combustion, *Combust. Flame* 154 (2008) 546–556.
- [8] B. Wang, Q. Eri, T. Li, R. Duan, Experimental investigation on the effect of oxygen enhancement on radiation distribution in inverse diffusion flames, *ASME 2016 International Mechanical Engineering Congress and Exposition* (2016) paper V008T10A024.
- [9] Z. Wang, P.B. Sunderland, R.L. Axelbaum, Dilution effects on laminar jet diffusion flame lengths, *Proc. Combust. Inst.* 37 (2019) 1547–1553.
- [10] C.J. Sung, D.L. Zhu, C.K. Law, On micro-buoyancy spherical diffusion flames and a double blue zone structure of the hydrogen/methane flame, *Symp. (Int.) Combust.* 27 (1998) 2559–2566.
- [11] P.B. Sunderland, R.L. Axelbaum, D.L. Urban, B.H. Chao, S. Liu, Effects of structure and hydrodynamics on the sooting behavior of spherical microgravity diffusion flames, *Combust. Flame* 132 (2003) 25–33.
- [12] P.B. Sunderland, D.L. Urban, D.P. Stocker, B.-H. Chao, R.L. Axelbaum, Sooting limits of microgravity spherical diffusion flames in oxygen-enriched air and diluted fuel, *Combust. Sci. Technol.* 176 (2004) 2143–2164.
- [13] A. Markan, P.B. Sunderland, J.G. Quintiere, J.L. de Ris, D.P. Stocker, H.R. Baum, A burning rate emulator (BRE) for study of condensed fuel burning in microgravity, *Combust. Flame* 192 (2018) 272–282.
- [14] H.I. Joo, Ö.L. Gülder, Soot formation and temperature structure in small methane–oxygen diffusion flames at subcritical and supercritical pressures, *Combust. Flame* 157 (2010) 1194–1201.
- [15] P.H. Joo, M.R.J. Charest, C.P.T. Groth, Ö.L. Gülder, Comparison of structures of laminar methane–oxygen and methane–air diffusion flames from atmospheric to 60 atm, *Combust. Flame* 160 (2013) 1990–1998.

- [16] K. Saito, F.A. Williams, A.S. Gordon, Structure of laminar coflow methane air diffusion flames, *J. Heat Transf.* 108 (1986) 640–648.
- [17] Z. Diao, M. Winter, T. Hirasawa, Y. Kato, Y. Ishino, K. Saito, Characterization of six clustered methane-air diffusion microflames through spectroscopic and tomographic analysis of CH^* and C_2^* chemiluminescence, *Exp. Therm. Fluid Sci.* 102 (2019) 20–27.
- [18] F. Weinberg, F. Carleton, Ionization and chemiluminescence during the progressive aeration of methane flames, *Combust. Flame* 156 (2009) 2276–2284.
- [19] F. Weinberg, F. Carleton, R. Houdmont, D. Dunn-Rankin, S. Karnani, Syngas formation in methane flames and carbon monoxide release during quenching, *Combust. Flame* 158 (2011) 273–280.
- [20] K.C. Smyth, J.H. Miller, R.C. Dorfman, W.G. Mallard, R.J. Santoro, Soot inception in a methane/air diffusion flame as characterized by detailed species profiles, *Combust. Flame* 62 (1985) 157–181.
- [21] M.D. Smooke, Y. Xu, R.M. Zurn, P. Lin, J.H. Frank, M.B. Long, Computational and experimental study of OH and CH radicals in axisymmetric laminar diffusion flames, *Symp. (Int.) Combust.* 24 (1992) 813–821.
- [22] R.E. Mitchell, A.F. Sarofim, L.A. Clomburg, Experimental and numerical investigation of confined laminar diffusion flames, *Combust. Flame* 37 (1980) 227–244.
- [23] K.T. Wu, R.H. Essenhigh, Mapping and structure of inverse diffusion flames of methane, *Symp. (Int.) Combust.* 20 (1984) 1925–1932.
- [24] K. Seshadri, N. Ilincic, The asymptotic structure of nonpremixed methane-air flames with oxidizer leakage of order unity, *Combust. Flame* 101 (1995) 69–80.
- [25] K. Seshadri, Multistep asymptotic analyses of flame structures, *Symp. (Int.) Combust.* 26 (1996) 831–846.
- [26] F.A. Williams, Progress in knowledge of flamelet structure and extinction, *Prog. Energy Combust. Sci.* 26 (2000) 657–682.
- [27] S. Venkatesh, A. Ito, K. Saito, I.S. Wichman, Flame base structure of small-scale pool fires, *Symp. (Int.) Combust.* 26 (1996) 1437–1443.
- [28] J.M. Samaniego, F.N. Egofoopoulos, C.T. Bowman, CO_2^* chemiluminescence in premixed flames, *Combust. Sci. Technol.* 109 (1995) 183–203.
- [29] T.F. Guiberti, D. Durox, T. Schuller, Flame chemiluminescence from CO_2 - and N_2 -diluted laminar CH_4 /air premixed flames, *Combust. Flame* 181 (2017) 110–122.
- [30] L. Merotto, M.S. Irignano, M. Commoco, A. D'Anna, R. Dondè, S. De Iulii, Experimental characterization and modeling for equivalence ratio sensing in non-premixed flames using chemiluminescence and laser-induced breakdown spectroscopy techniques, *Energy Fuel* 31 (2017) 3227–3233.
- [31] K. Wang, F. Li, F. Wu, X. Yu, Quantitative measurements of chemiluminescence in a laminar methane-air premixed flame and comparison to numerical methods, *Energy Fuel* 32 (2018) 5536–5543.
- [32] J.J. Kojima, Y. Ikeda, T. Nakajima, Spatially resolved measurement of OH^* , CH^* , and C_2^* chemiluminescence in the reaction zone of laminar methane/air premixed flames, *Proc. Combust. Inst.* 28 (2000) 1757–1764.
- [33] D. Giassi, S. Cao, B.A.V. Bennett, D.P. Stocker, F. Takahashi, M.D. Smooke, M.B. Long, Analysis of CH^* concentration and flame heat release rate in laminar coflow diffusion flames under microgravity and normal gravity, *Combust. Flame* 167 (2016) 198–206.
- [34] T. Zhang, Q. Guo, X. Song, Z. Zhou, G. Yu, The chemiluminescence and structure properties of normal/inverse diffusion flames, *J. Spectrosc.* 2013 (2013) 1–7.
- [35] H. Zhu, C. Hu, Q. Guo, Y. Gong, G. Yu, Investigation on chemiluminescence and structure characteristics in CH_4/O_2 diffusion flames, *Exp. Therm. Fluid Sci.* 102 (2019) 595–602.
- [36] H. Guo, J.A. Castillo, P.B. Sunderland, Digital camera measurements of soot temperature and soot volume fraction in axisymmetric flames, *Appl. Opt.* 52 (2013) 8040–8047.
- [37] D. De Sousa Meneses, P. Melin, L. del Campo, L. Cosson, P. Echegut, Apparatus for measuring the emittance of materials from far infrared to visible wavelengths in extreme conditions of temperature, *Infrared Phys. Technol.* 69 (2015) 96–101.
- [38] P.B. Kuhn, B. Ma, B.C. Connelly, M.D. Smooke, M.B. Long, Soot and thin-filament pyrometry using a color digital camera, *Proc. Combust. Inst.* 33 (2011) 743–750.
- [39] B. Ma, G. Wang, G. Magnotti, R.S. Barlow, M.B. Long, Intensity-ratio and color-ratio thin-filament pyrometry: uncertainties and accuracy, *Combust. Flame* 161 (2014) 908–916.
- [40] C.J. Dasch, One-dimensional tomography of Abel, onion-peeling, and filtered backprojection methods, *Appl. Opt.* 31 (1992) 1146–1152.
- [41] H. Guo, Soot oxidation in hydrocarbon-free flames, University of Maryland Dissertation (2015).
- [42] Z.G. Yuan, The filtered Abel transform and its application in combustion diagnostics, Western States Section of the Combustion Institute Fall Technical Meeting (1995).
- [43] K.J. Daun, K.A. Thomson, F. Liu, G.J. Smallwood, Deconvolution of axisymmetric flame properties using Tikhonov regularization, *Appl. Opt.* 45 (2006) 4638–4646.
- [44] M.A. Mikofski, T.C. Williams, C.R. Shaddix, L.G. Blevins, Flame height measurement of laminar inverse diffusion flames, *Combust. Flame* 146 (2006) 63–72.
- [45] F. Escudero, A. Fuentes, R. Demarco, J.L. Consalvi, F. Liu, J.C. Elicer-Cortés, C. Fernandez-Pello, Effects of oxygen index on soot production and temperature in an ethylene inverse diffusion flame, *Exp. Therm. Fluid Sci.* 73 (2016) 101–108.
- [46] A. Lock, A.M. Briones, S.K. Aggarwal, I.K. Puri, U. Hegde, Liftoff and extinction characteristics of fuel-and air-stream-diluted methane-air flames, *Combust. Flame* 149 (2007) 340–352.
- [47] A. Lock, S.K. Aggarwal, I.K. Puri, Effect of fuel type on the extinction of fuel and air stream diluted partially premixed flames, *Proc. Combust. Inst.* 32 (2009) 2583–2590.
- [48] Z. Shu, B.J. Krass, C.W. Choi, S.K. Aggarwal, V.R. Katta, I.K. Puri, An experimental and numerical investigation of the structure of steady two-dimensional partially premixed methane-air flames, *Symp. (Int.) Combust.* 27 (1998) 625–632.
- [49] R. Azzoni, S. Ratti, S.K. Aggarwal, I.K. Puri, The structure of triple flames stabilized on a slot burner, *Combust. Flame* 119 (1999) 23–40.
- [50] S.K. Aggarwal, Extinction of laminar partially premixed flames, *Prog. Energy Combust. Sci.* 35 (2009) 528–570.